applied sciences

MDPI

Article

Design and Multi-Objective Optimization of an Asymmetric-Rotor Permanent-Magnet-Assisted Synchronous Reluctance Motor for Improved Torque Performance

Feng Xing [1], Jiajia Zhang [1], Mingming Zhang [2] and Caiyan Qin [2,*]

[1] School of Electrical Engineering, Liaoning University of Technology, Jinzhou 121001, China
[2] School of Mechanical Engineering and Automation, Harbin Institute of Technology, Shenzhen 518055, China
* Correspondence: qincaiyan@hit.edu.cn

Abstract: Permanent-magnet-assisted synchronous reluctance motors (PMA-SynRMs) are widely used in modern industry as a kind of electromagnetic energy conversion device with high output torque, high power density, high efficiency, and excellent speed regulation. In this paper, an asymmetric-rotor PMA-SynRM combined with a Halbach array is proposed based on the conventional PMA-SynRM without modifying the amount of permanent magnet. With the finite element no-load analysis, it is proven that the permanent magnet arrangement of this method can achieve better flux focusing effect and magnetic-axis-shift (MAS) effect. A significant increase and shift of the air-gap magnetic density has also been observed. Meanwhile, the load simulation demonstrated that the proposed model possesses higher utilization of permanent magnet torque and reluctance torque compared to the conventional model. In addition, a multi-objective optimization has been performed for the rotor structure of the proposed model, and the optimized model improved the average torque by 25.32% and reduced the torque ripple by 76.92% compared to the conventional model. Finally, the constant power speed range (CPSR) performance and anti-demagnetization performance have been analyzed for the three models. The results showed that the proposed and optimized models performed better on constant power speed range, and all three models of permanent magnets had good anti-demagnetization performance. The maximum demagnetization rate of the optimized model is reduced by 13.84% compared to the proposed model at an operating condition of 200 °C and nine times the rated current.

Keywords: PMA-SynRM; torque; asymmetric rotor; MAS; multi-objective optimization

Citation: Xing, F.; Zhang, J.; Zhang, M.; Qin, C. Design and Multi-Objective Optimization of an Asymmetric-Rotor Permanent-Magnet-Assisted Synchronous Reluctance Motor for Improved Torque Performance. *Appl. Sci.* **2024**, *14*, 6734. https://doi.org/10.3390/app14156734

Academic Editor: Frede Blaabjerg

Received: 9 July 2024
Revised: 25 July 2024
Accepted: 30 July 2024
Published: 1 August 2024

1. Introduction

Recently, due to the increasing consumption of rare earth resources, the prices of various raw materials such as rare earths have been increasing [1,2]. Since rare earth is a non-renewable resource, in order to reduce the dependence on rare earth resources, permanent-magnet-assisted synchronous reluctance motors (PMA-SynRMs) are gradually entering into the public's view [3]. The PMA-SynRM combines the advantages of permanent magnet synchronous motors (PMSMs) and synchronous reluctance motors, characterized by high output torque, high power density, high efficiency, and good speed regulation performance [4,5]. A multilayer flux barrier structure is generally applied in the PMA-SynRMs to maximize the utilization of their reluctance torque [6,7]. Only a small amount of permanent magnets remains in the flux barrier structure of the PMA-SynRM to assist the excitation [8,9], which provides permanent magnet torque for the PMA-SynRM. The PMA-SynRM typically utilizes fewer permanent magnet compared to PMSM for the same volume of PMA-SynRM [10,11]. Therefore, the cheaper price and better performance give the PMA-SynRM a wide range of applications in the field of variable speed drives for electric vehicles, water pump compressors, household appliances, medical devices, etc. [12–17].

Currently, the research for PMA-SynRM topology is centered on the design of the flux barrier structure, permanent magnet, and magnetic circuit [18,19]. In the design of the flux barrier structure, a variety of flux barrier structures such as U-shaped flux barrier, V-shaped flux barrier, and arc-shaped flux barrier have been proposed [20,21]. N. Bianchi's team [22] at the University of Padua effectively reduced the torque ripple of the PMA-SynRM by axially combining two rotors with different flux barrier angles. In terms of permanent magnet design, different numbers, volumes, shapes, arrangements, and magnetization directions of permanent magnets have been proven to have an impact on the torque performance of the PMA-SynRM [23,24]. Huaicong Liu et al. [25] in Korea investigated the effect of different arrangements of permanent magnets within the flux barrier and found that the PMA-SynRM had the smallest torque ripple when the permanent magnets were all located in the middle of the flux barrier. Chengwu Diao et al. [26], from Shandong University, China, designed a pole-biased PMA-SynRM to enhance the torque of the PMA-SynRM by varying the angle between the permanent magnet flux linkage and the *d-axis*, so that both the permanent magnet torque and the reluctance torque are maximized at the same current phase angle. Ying Xie et al. [27], from Harbin University of Science and Technology, China, similarly improved the utilization of the reluctance torque and the permanent magnet torque by mixing NdFeB and Ferrite permanent magnets of different sizes, which resulted in an offset of the permanent magnet chain.

The conventional PMA-SynRM permanent magnet arrangement is less efficient in utilizing the magnetic force of the permanent magnets. Without modifying the amount of permanent magnet, an asymmetric-rotor PMA-SynRM model with magnetic-axis-shift (MAS) effect is proposed in this paper in combination with a Halbach array. This permanent magnet arrangement not only enhances the permanent magnet auxiliary excitation effect of the PMA-SynRM but also offsets the permanent magnet chain. The permanent magnet torque and reluctance torque of the proposed model can reach their maximum value with a similar current phase angle, and the total torque is significantly improved.

Firstly, the stator–rotor topology of the conventional and proposed models is presented in this paper. The torque characteristics of the two models are theoretically analyzed by building a simplified analytical model of the two models, with core saturation and cross-coupling neglected. The two models are also simulated and analyzed under no-load conditions as well as under load conditions based on the finite element method. In this paper, all models are simulated by using JMAG finite element analysis software (v.21.0). Under no-load conditions, the permanent magnet flux linkage of the proposed model is significantly shifted compared with the conventional model, and the flux aggregation effect of the permanent magnet arrangement combined with a Halbach array is significant. The air-gap flux density and the back electromotive force (EMF) are significantly shifted and increased compared to the conventional model. The torque decomposition of the conventional and proposed models is conducted using the frozen permeability method under loaded operating conditions. The proposed model has the MAS effect, and the permanent magnet torque and the reluctance torque can be maximized at similar current phase angles. Compared to the conventional model, the proposed model has higher permanent magnet torque utilization and reluctance torque utilization. Next, this paper optimizes the rotor topology of the proposed model based on the FAST multi-objective optimization algorithm in modeFRONTIER. The optimized model has higher average torque and lower torque ripple than the conventional and the proposed models. Finally, the constant power speed range (CPSR) performance and anti-demagnetization performance are analyzed for the three models. The comparison results of CPSR performance show that the proposed model and optimized model have better CPSR performance. In the anti-demagnetization performance analysis, it is shown that all three models have good anti-demagnetization performance. In comparison, the permanent magnets of the conventional model have better anti-demagnetization performance, while the permanent magnets of the proposed model have worse anti-demagnetization performance.

Due to the low average torque of conventional PMA-SynRM, in this paper, an asymmetric-rotor PMA-SynRM motor model combined with a Halbach array is proposed based on the above study. The sections of the article are organized as follows: In Section 2, the conventional model as well as the motor topology of the proposed model are presented. A comparative analysis of the two models at no-load and load conditions is also carried out to demonstrate the torque characteristics and torque improvement of the proposed model. In Section 3, the torque performance of the motor is optimized by changing the rotor topology of the proposed model, and the optimal design, sensitivity analysis, and multi-objective optimization are carried out. In Section 4, the CPSR performance and anti-demagnetization performance of the three models are analyzed. In Section 5, a short summary is provided.

2. Motor Topology and Simulation Analysis

The topologies of the conventional and proposed models are presented along with the specification parameters. The two motor models were also analyzed by finite element simulation under no-load and load conditions.

2.1. Motor Topology

In this paper, a conventional PMA-SynRM model is used as a conventional model and an asymmetric-rotor PMA-SynRM model combined with a Halbach array is the proposed model. Both models are eight-pole, 48-slot PMA-SynRMs with a three-layer U-shaped magnetic barrier and roughly the same amount of steel sheets. Meanwhile, the stator structure and winding configuration are the same for both models. The windings are configured as distributed windings. The amount of permanent magnets inside the rotor is also consistent between the conventional and proposed models. The topology of the stator–rotor for the conventional and proposed models in this paper is shown in Figure 1. The direction of the black arrows in Figure 1a,c indicate the direction of magnetization of the permanent magnet. The specific parameters of the two models are shown in Table 1.

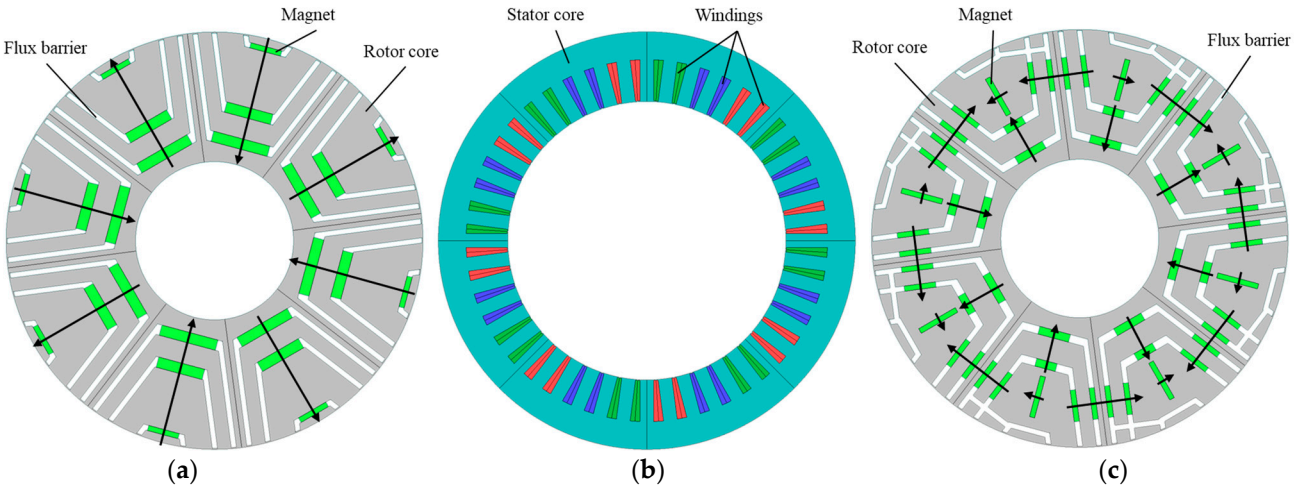

Figure 1. Stator and rotor topologies for the conventional and proposed models. (**a**) The rotor topology of the conventional model. (**b**) Stator and winding topology. (**c**) The rotor topology of the proposed model.

In order to study the MAS effect of the proposed model, a simplified analytical model of the conventional and proposed models neglecting core saturation and cross-coupling is developed based on the single-pole planar expansion of the rotor shown in Figure 2. From Figure 2b, it can be seen that the permanent magnet flux linkage ψ_{pm} of the proposed model has been shifted, and ψ_{pm} forms an angle α with the *d-axis*. The simplified vector diagram built from Figure 2 is shown in Figure 3.

Table 1. Dimensional parameters of the conventional and proposed models.

Item	Unit	Conv. Model/Prop. Model
Pole/Slot	/	8/48
Stator outer diameter	mm	120
Stator inner diameter	mm	80
Rotor outer diameter	mm	79
Rotor inner diameter	mm	30
Air-gap length	mm	0.5
Motor axial length	mm	140
Permanent magnet	/	NdFeB
Permanent magnet volume	mm^3	52640
Steel sheet	/	50JN1300

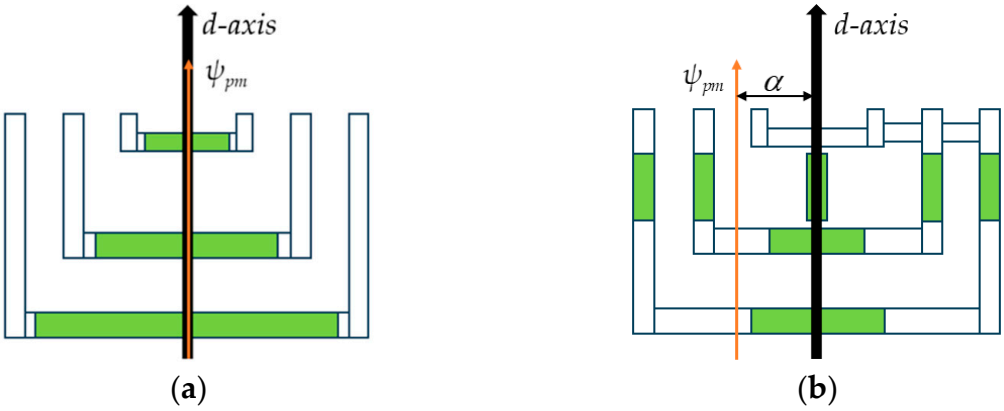

Figure 2. Single-pole planar expansion of the two model rotors. (**a**) Conventional model plan view. (**b**) Proposed model plan view.

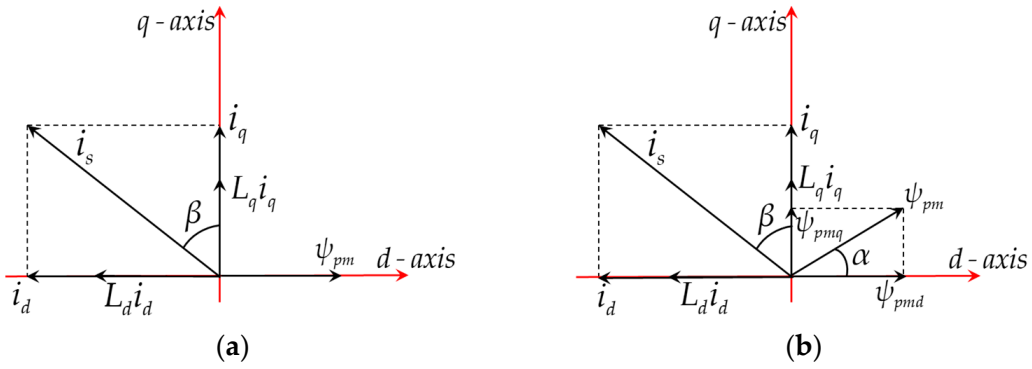

Figure 3. Simplified vector diagrams of the two models. (**a**) Conventional model vector diagram. (**b**) Proposed model vector diagram.

From Figure 3a, it can be seen that the *d-axis* magnetic flux linkage generated by the current in the stator is in the opposite direction to the permanent magnet flux linkage. Based on the constant coordinate transformation of the magnetic potential, the magnetic flux linkage in the conventional model with respect to the *d-axis* and *q-axis* can be expressed by Equation (1) [27].

$$\begin{cases} \psi_d = \psi_{pm} + L_d i_d = \psi_{pm} - L_d i_s sin\beta \\ \psi_q = L_q i_q = L_q i_s cos\beta \end{cases} \quad (1)$$

where ψ_{pm}, ψ_d, and ψ_q are the permanent magnet flux linkage, the *d-axis* linkage, and the *q-axis* linkage, respectively; L_d and L_q are the *d-axis* inductance and the *q-axis* inductance, respectively; i_d and i_q are the *d-axis* current and the *q-axis* current, respectively; i_s is the current in the stator; and β is the angle between the current i_s in the stator and the *d-axis*.

According to Equation (1), the torque formula for the conventional model can be obtained as shown in Equation (2).

$$\begin{aligned} T_{E1} &= \tfrac{3}{2}p(\psi_d i_q - \psi_q i_d) \\ &= \tfrac{3}{2}p(\psi_{pm} i_q + (L_d - L_q) i_d i_q) \\ &= \tfrac{3}{2}p\psi_{pm} i_s cos\beta + \tfrac{3}{4}p(L_q - L_d) i_s^2 sin(2\beta) \\ &= T_{PM1} + T_{RE1} \end{aligned} \tag{2}$$

where T_{E1}, T_{PM1}, and T_{RE1} are the total torque, permanent magnet torque, and reluctance torque of the conventional model, respectively, and p is the pole-pair number.

Since the proposed model is an asymmetric rotor, in this particular arrangement of the permanent magnets, the permanent magnet flux linkage ψ_{pm} shifts and forms an angle of α with the *d-axis* as shown in Figure 3b. Based on the constant coordinate transformation of the magnetic potential, the magnetic flux linkages in the proposed model with regard to the *d-axis* and *q-axis* can be expressed by Equation (3) [27].

$$\begin{cases} \psi_d = \psi_{pmd} + L_d i_d = \psi_{pm} cos\alpha - L_d i_s sin\beta \\ \psi_q = \psi_{pmq} + L_q i_q = \psi_{pm} sin\alpha + L_d i_s cos\beta \end{cases} \tag{3}$$

where ψ_{pmd} and ψ_{pmq} are the *d-axis* and *q-axis* permanent magnet flux linkages, respectively.

According to Equation (3), the torque formula of the proposed model can be obtained as shown in Equation (4).

$$\begin{aligned} T_{E2} &= \tfrac{3}{2}p(\psi_d i_q - \psi_q i_d) \\ &= \tfrac{3}{2}p(\psi_{pmd} i_q - \psi_{pmq} i_d + (L_d - L_q) i_d i_q) \\ &= \tfrac{3}{2}p\psi_{pm} i_s cos(\beta - \alpha) + \tfrac{3}{4}p(L_q - L_d) i_s^2 sin(2\beta) \\ &= T_{PM2} + T_{RE2} \end{aligned} \tag{4}$$

where T_{E2}, T_{PM2}, and T_{RE2} are the total torque, permanent magnet torque, and reluctance torque of the proposed model, respectively.

By analyzing Equation (4), it is found that the permanent magnet torque and the reluctance torque of the proposed model can reach their peak values at the same current phase angle when the angles β and α satisfy the following equations. The relationship between angle β and α is shown in Equation (5).

$$\alpha = \beta = \frac{\pi}{4} \tag{5}$$

Substituting Equation (5) into Equation (3) yields the theoretical peak torque formula for the proposed model as shown in Equation (6).

$$\begin{aligned} T_{E2MAX} &= \tfrac{3}{2}p\psi_{pm} i_s + \tfrac{3}{4}p(L_q - L_d) i_s^2 \\ &= T_{PM2MAX} + T_{RE2MAX} \end{aligned} \tag{6}$$

where T_{E2MAX}, T_{PM2MAX}, and T_{RE2MAX} are the theoretical maximum total torque, permanent magnet torque, and reluctance torque of the proposed model, respectively.

By comparing Equations (2) and (5), it is found that the permanent magnet torque and the reluctance torque of the conventional model can never both reach their maximum values at the same current phase angle. The proposed model with the MAS effect can theoretically maximize the permanent magnet torque and reluctance torque at the same or a similar current phase angle, resulting in a higher total superimposed torque.

2.2. Simulation Analysis for No-Load Condition

In order to verify the MAS effect and the flux aggregation effect of the proposed model, the simulation analyses of the two models were carried out under no-load conditions. Figure 4 shows the flux line distribution of the conventional model and the proposed

model under no-load condition. After comparison, it is found that the permanent magnet flux linkage ψ_{pm} of the proposed model is shifted and forms an angle of α with the *d-axis*. The proposed model utilizes a permanent magnet at the center of the rotor single-pole to achieve the magnetic field deflection inside the rotor, shielded from flux by a connected flux barrier on the right side of the rotor single-pole. By comparing Figure 4a,b, it is found that the inner flux line density of the rotor of the proposed model is lower, while the flux line density in the stator is higher, which is consistent with the properties of the Halbach array. The proposed model incorporates the permanent magnet arrangement of the Halbach array, which makes the permanent-magnet-assisted excitation more effective. The higher density of flux lines in region A of Figure 4b for the proposed model indicates that the proposed model has a better flux aggregation effect.

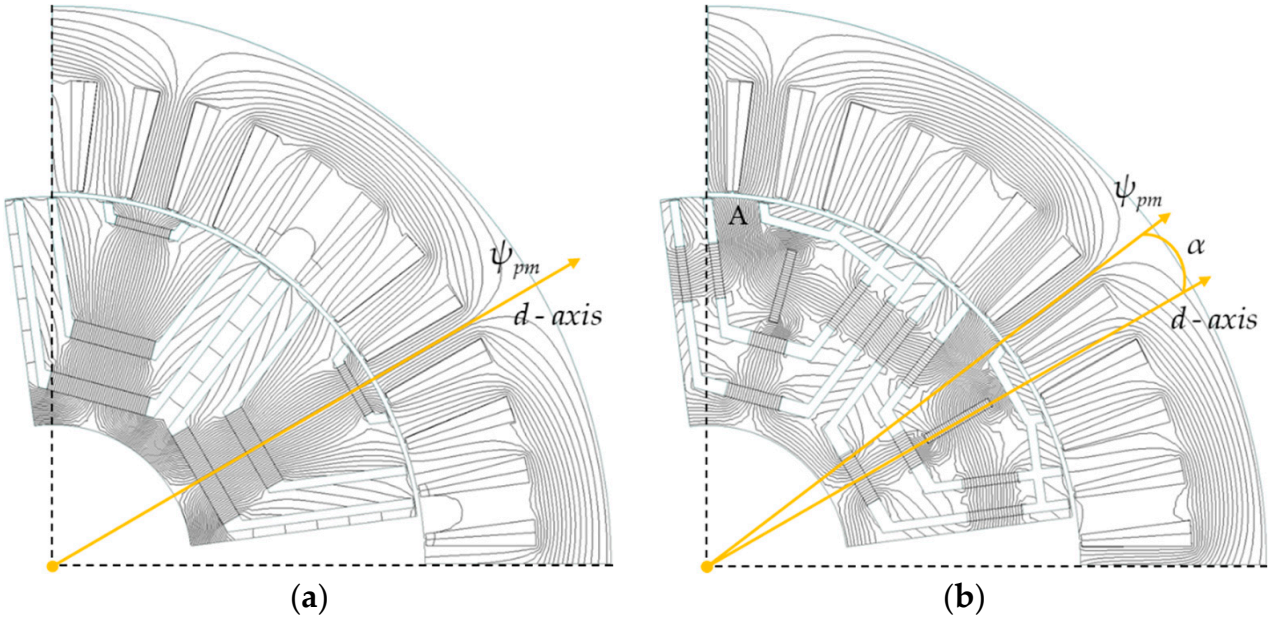

Figure 4. Flux line distribution plots for both models under no-load conditions. (**a**) Conventional model. (**b**) Proposed model.

Figure 5 demonstrates the comparison of the no-load air-gap flux density between the conventional model and the proposed model. According to Figure 5a, it can be seen that the air-gap flux density magnitude of the proposed model is higher than those of the conventional model, and its air-gap flux density RMS is improved by 32.43% compared with the conventional model. Based on the air-gap flux density waveforms, it can be seen that the proposed model produces a certain offset angle compared to the conventional model. According to Figure 5b, due to the asymmetric structure of the proposed model, the higher harmonics in the harmonic decomposition of the air-gap flux density are larger compared to the conventional model, and there are obvious distortions. The no-load back-EMF waveforms and harmonic decomposition of the two models are shown in Figure 6. Consistent with the air-gap flux density waveforms, the magnitude of the back-EMF waveforms of the proposed model is higher compared to the conventional model, and there is a certain offset. From Figure 6b, it can be seen that the high harmonics of the back EMF of the proposed model are still larger than those of the conventional model, and distortions also appear.

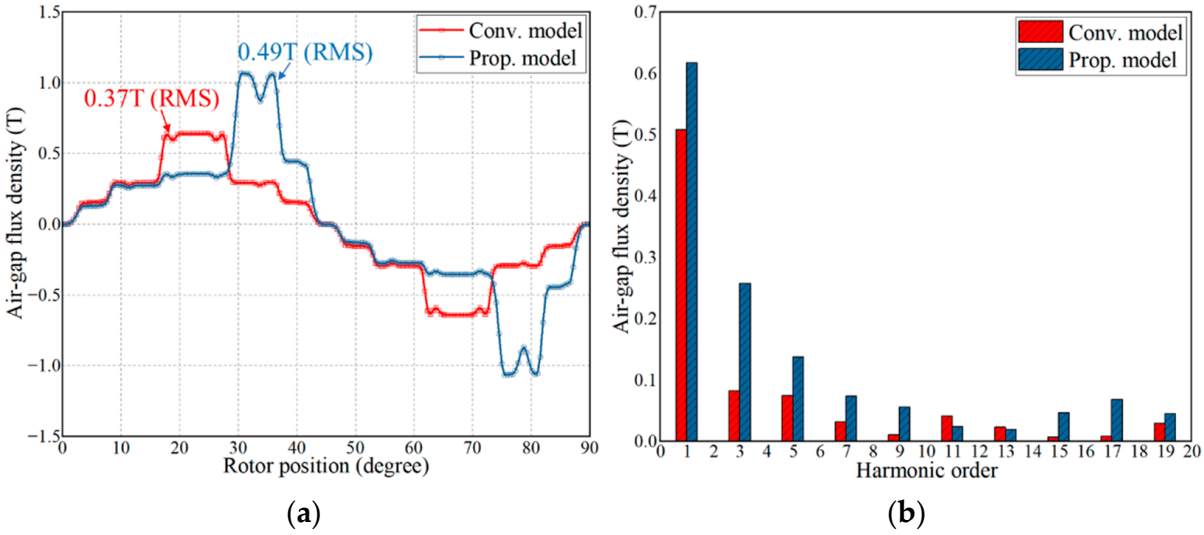

Figure 5. Comparison of no-load air-gap flux density for the two models. (**a**) Air-gap flux density waveform. (**b**) Harmonic decomposition of the air-gap flux density.

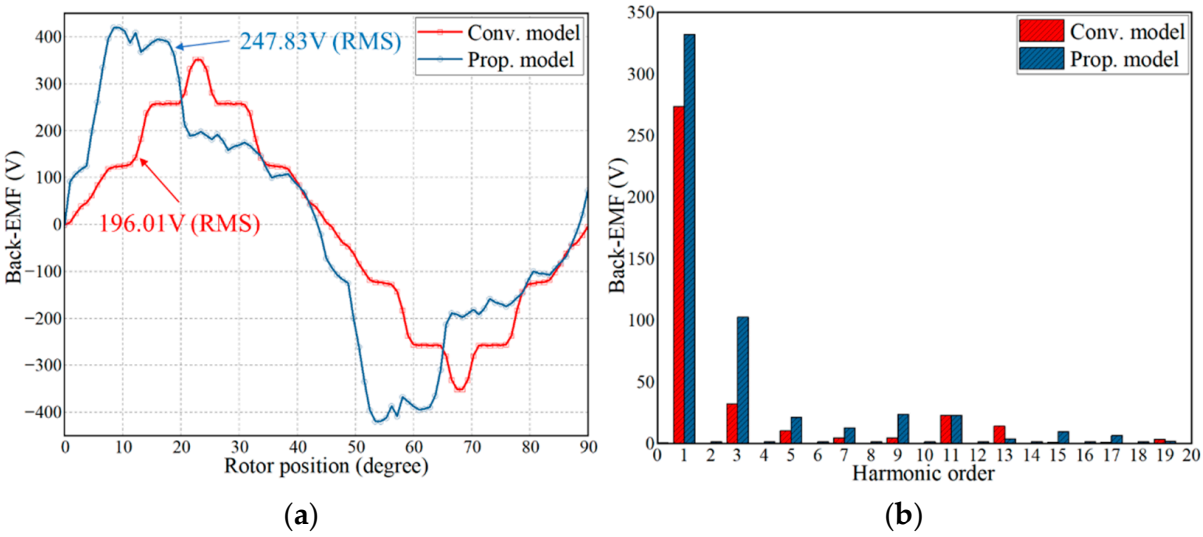

Figure 6. Comparison of no-load back EMF for the two models. (**a**) Back-EMF waveform. (**b**) Harmonic decomposition of back EMF.

2.3. Simulation Analysis for On-Load Condition

The torque of the PMA-SynRM consists mainly of permanent magnet torque and reluctance torque. In order to verify the torque characteristics of the proposed model after the MAS effect, the torque of the two models is decomposed using the frozen permeability method. The torque distribution of the two models at different current phase angles for a current RMS value of 2A is shown in Figure 7. It should be noted that in Figure 7, the orange markers are the components of the permanent magnet torque and the reluctance torque at the maximum total torque, and the green markers represent the components of the permanent magnet torque and the reluctance torque at the maximum total torque. The maximum total torque of the proposed model is improved by 22.3% compared to the conventional model. As seen in Figure 7a, the components of the maximum permanent magnet torque and the maximum reluctance torque of the conventional model have a phase difference of 45 degrees. In Figure 7b, the components of the maximum permanent magnet torque and the maximum reluctance torque of the proposed model display only 15 degrees

of phase difference. Permanent magnet torque and reluctance torque utilization can be expressed by Equation (7).

$$\begin{cases} \xi_{PM} = \frac{T_{PM}}{T_{PM\text{-}MAX}} \times 100\% \\ \xi_{RE} = \frac{T_{RE}}{T_{RE\text{-}MAX}} \times 100\% \end{cases} \tag{7}$$

where ξ_{PM} and ξ_{RE} are the permanent magnet torque utilization and the reluctance torque utilization, respectively; T_{PM} and T_{RE} are the permanent magnet torque and the reluctance torque components at the maximum total torque, respectively; and $T_{PM\text{-}MAX}$ and $T_{RE\text{-}MAX}$ are the maximum permanent magnet torque component and the maximum reluctance torque component, respectively.

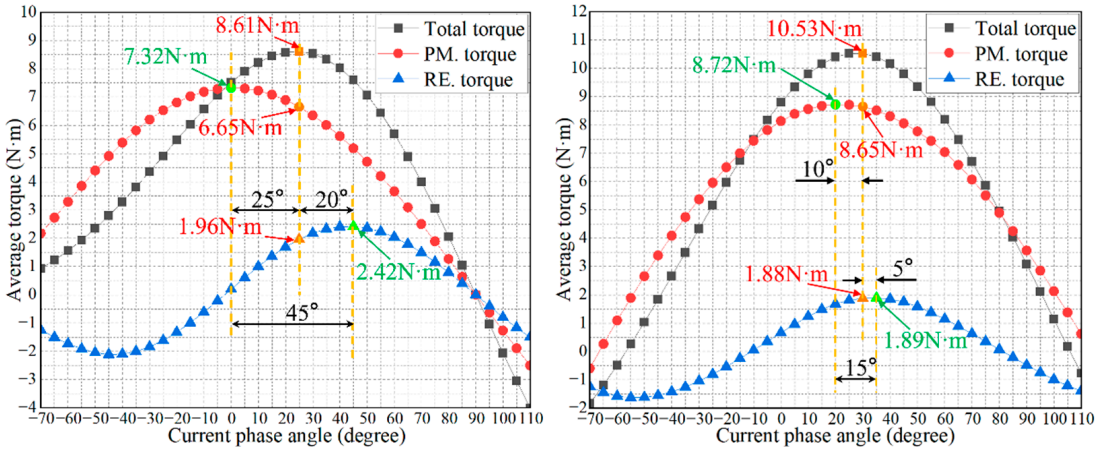

(**a**) (**b**)

Figure 7. Comparison of the torque characteristics of the two models. (**a**) Conventional model. (**b**) Proposed model.

From Table 2, it can be seen that the utilization of both permanent magnet torque and reluctance torque is higher in the proposed model compared to the conventional model. This proves that the proposed model with the MAS effect can shift the permanent magnet torque and reduce the phase difference between the permanent magnet torque and the reluctance torque. Figure 8 shows the flux density cloud diagrams of the conventional and proposed models under load conditions. From Figure 8, it can be seen that the flux density of the proposed model is significantly higher than that of the conventional model in flux circuit B.

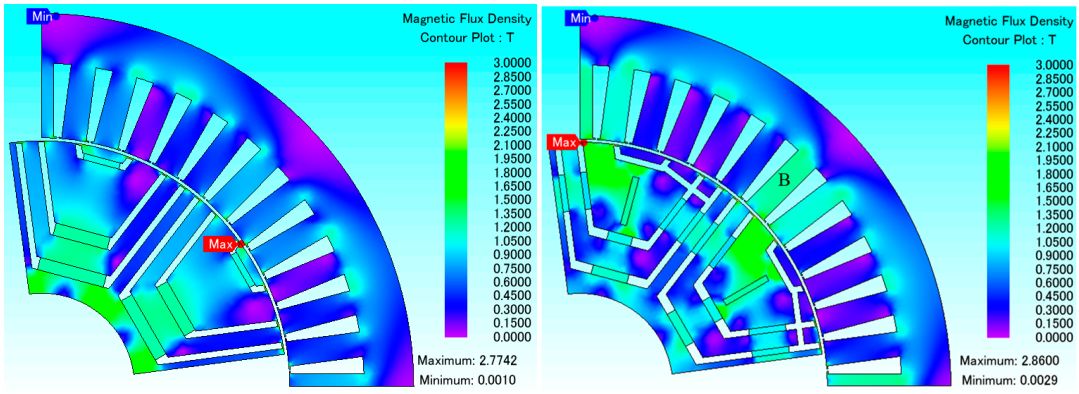

(**a**) (**b**)

Figure 8. Flux density cloud plots of the two models under load conditions. (**a**) Conventional model. (**b**) Proposed model.

Table 2. Comparison of torque characteristics of the conventional and proposed models.

Item	Unit	Conv. Model	Prop. Model
T_{PM}	N·m	6.65	8.65
$T_{PM\text{-}MAX}$	N·m	7.32	8.72
ξ_{PM}	%	90.85	99.20
T_{RE}	N·m	1.96	1.88
$T_{RE\text{-}MAX}$	N·m	2.42	1.89
ξ_{RE}	%	80.99	99.47

3. Multi-Objective Optimization of the Motor Topology

Firstly, a multi-objective optimization design was carried out. Secondly, a sensitivity analysis of the parameter variables involved in the optimization was carried out. Finally, a comparative analysis of the optimized results was carried out.

3.1. Multi-Objective Optimization Design

In order to obtain better torque performance for the proposed model in this paper, the average torque and torque ripple of the proposed model are optimized by changing the rotor topology of the proposed model. Figure 9 shows a parametric diagram of the single-pole topology of the proposed model rotor. Figure 10 shows the flowchart of multi-objective optimization. The optimization objectives of this multi-objective optimization are average torque and torque ripple. The definitions of average torque and torque ripple can be expressed by Equation (8).

$$\begin{cases} T_{ave} = \dfrac{\sum\limits_{i=1}^{n} T_i}{n} \\ T_{rip} = \dfrac{T_{max} - T_{min}}{T_{ave}} \times 100\% \end{cases} \tag{8}$$

where T_{ave} and T_{rip} are the average torque and torque ripple, respectively; n is the number of steps of the motor in one operating period; T_i is the torque at the i step; and T_{max} and T_{min} are the maximum torque and minimum torque of the motor in one operating period, respectively.

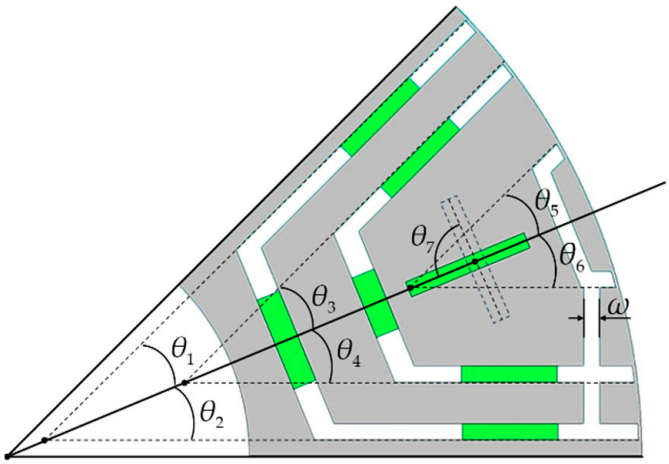

Figure 9. Parameter diagram of the single-pole topology of the proposed model rotor.

The average torque and torque ripple are taken as the optimization objectives, and the optimization objective function can be expressed by Equation (9).

$$\begin{cases} O_1 = max(T_{ave}) \\ O_2 = min(T_{rip}) \end{cases} \tag{9}$$

where O_1 and O_2 are the average torque optimization objective and torque ripple optimization objective, respectively.

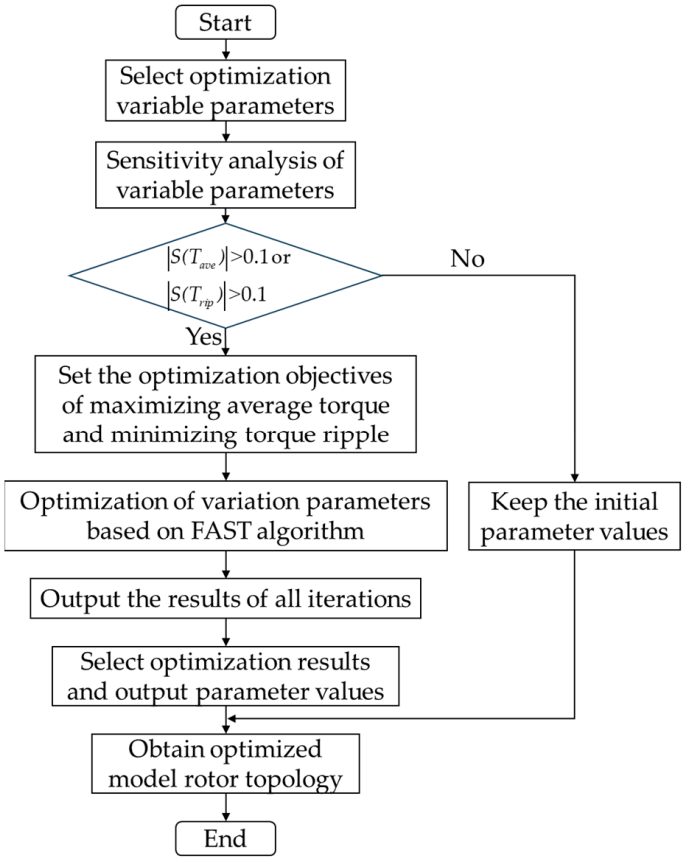

Figure 10. Flowchart of the multi-objective optimization.

The constraint function in multi-objective optimization can be represented by Equation (10).

$$s.t.\begin{cases} 20 \le \theta_k \le 25, k = 1,2,3,4,5,6 \\ 0 \le \theta_7 \le 90 \\ 1 \le \omega \le 2 \\ C_1 = T_{ave} - 10.5 \ge 0 \\ C_2 = T_{rip} - 0.1 \le 0 \end{cases} \tag{10}$$

where θ_k is the flux barrier angle; θ_7 is the deflection angle of the rotor's single-pole-centered permanent magnet; ω is the width of the connected flux barrier; and C_1 and C_2 are the constraint functions for the average torque and torque ripple.

3.2. Sensitivity Analysis

The Pearson correlation coefficient was used as a measure for this sensitivity analysis. The Pearson correlation coefficient captures the strength of the linear relationship between two variables with a coefficient interval of [−1,1]. When the absolute value of the Pearson correlation coefficient is closer to 1, it means that the correlation between the two variables is stronger; otherwise, the opposite is true. Let a set of random variables be (*A*,*B*), the Pearson correlation coefficient is calculated as shown in Equation (11) [28].

$$S = \frac{\sum_i (a_i - \bar{a}_i)(b_i - \bar{b}_i)}{\sqrt{\sum_i (a_i - \bar{a}_i)^2 (b_i - \bar{b}_i)^2}} \tag{11}$$

where $\overline{a}_i$ and $\overline{b}_i$ are the average of the random variable A and the average of the random variable B, respectively.

Using the Latin square sampling method, 100 sets of data were extracted for correlation analysis, and the results are shown in Figure 11. Variation parameters with absolute coefficient values of less than 0.1 will be removed in subsequent multi-objective optimization, and the original parameters will remain unchanged due to their low relevance to the optimization objective. From Figure 11, it can be seen that the absolute values of the correlation coefficients of θ_4 and ω with the average torque and torque ripple are less than 0.1, which means that these parameters will remain constant.

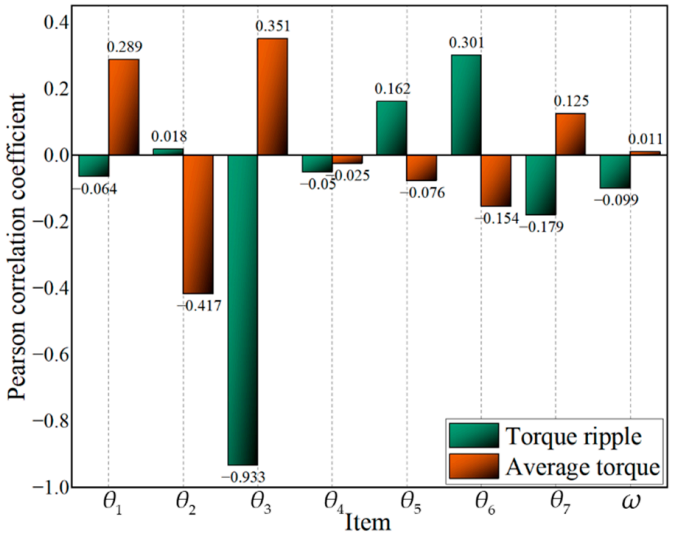

Figure 11. Sensitivity analysis results.

3.3. Multi-Objective Optimization and Torque Performance Comparison

Multi-objective optimization of the rotor topology of the proposed model is performed based on the FAST algorithm [29] in modeFRONTIER. Several multi-objective optimization algorithms in modeFRONTIER are compared in reference [29]. The FAST algorithm uses Response Surface Model (RSM) to speed up the optimization process. The optimization process is faster and the optimization search is better. Therefore, in this paper, the FAST algorithm is chosen for multi-objective optimization.

The FAST algorithm uses a self-initialization setting and limits the maximum number of iterations to 500. The optimized results are shown in Figure 12. In order to prevent the occurrence of excessive low average torque and excessive torque ripple, the frontier result in Figure 12 is selected as the optimized result through comprehensive consideration. The selection result is visible in the partially enlarged view of Figure 12. The dimensional parameters of the optimized model are shown in Table 3. Figure 13 shows the optimized model rotor single-pole topology of the model. The torques of the three models are shown in Figure 14. From Figure 14, it can be seen that the torque of the optimized model is the largest among the three models and has the least fluctuation. From Table 4, it can be seen that the optimized model improves the average torque by 25.32% and reduces the torque ripple by 76.92% compared to the conventional model. After multi-objective optimization, the torque performance of the optimized model is improved.

Table 3. Optimized topology parameters of the model rotor.

Name	Item	Unit	Value
Flux barrier angle 1	θ_1	degree	25.0
Flux barrier angle 2	θ_2	degree	20.0
Flux barrier angle 3	θ_3	degree	25.0
Flux barrier angle 4	θ_4	degree	22.5

Table 3. *Cont.*

Name	Item	Unit	Value
Flux barrier angle 5	θ_5	degree	22.1
Flux barrier angle 6	θ_6	degree	20.0
PM deflection angle	θ_7	degree	5.0
Connected flux barrier width	ω	mm	1.0

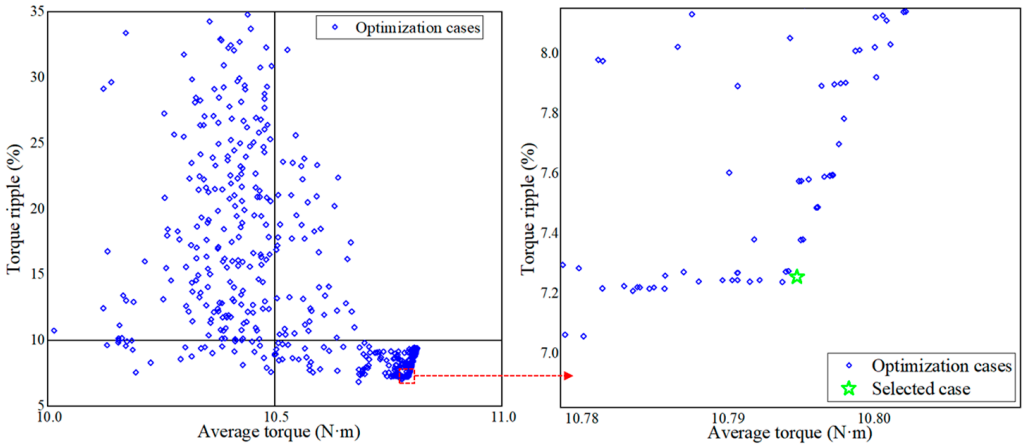

Figure 12. Results from the multi-objective optimization.

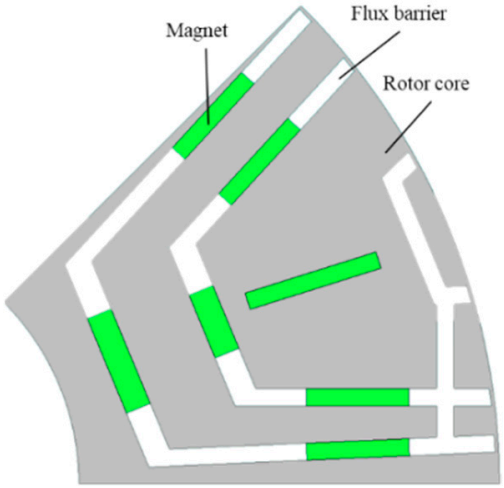

Figure 13. Optimized model rotor with single-pole topology.

Table 4. Comparison of torque performance of the three models.

Item	Unit	Conv. Model	Prop. Model	Opti. Model
Average torque	N·m	8.61	10.53	10.79
Torque ripple	%	31.50	18.19	7.27

Normally, in the design of the motor ontology, there is some error between the results of finite element simulation and the experimental results. References [12,14,30,31] gave finite element simulation results and experimental results for the output torque errors as shown in Table 5. In Table 5, the output torque errors in all references are less than 4.5% and the average error is 2.93%. Therefore, the errors between the finite element simulation results and the experimental results are much lower in the design of the motor ontology. In this paper, the average torque improvement of the optimized model is far higher than

the average error compared to the conventional model. It can be inferred that the errors do not have much effect on the finite element simulation results in this paper, and that the comparison of the finite element simulation results is still reliable.

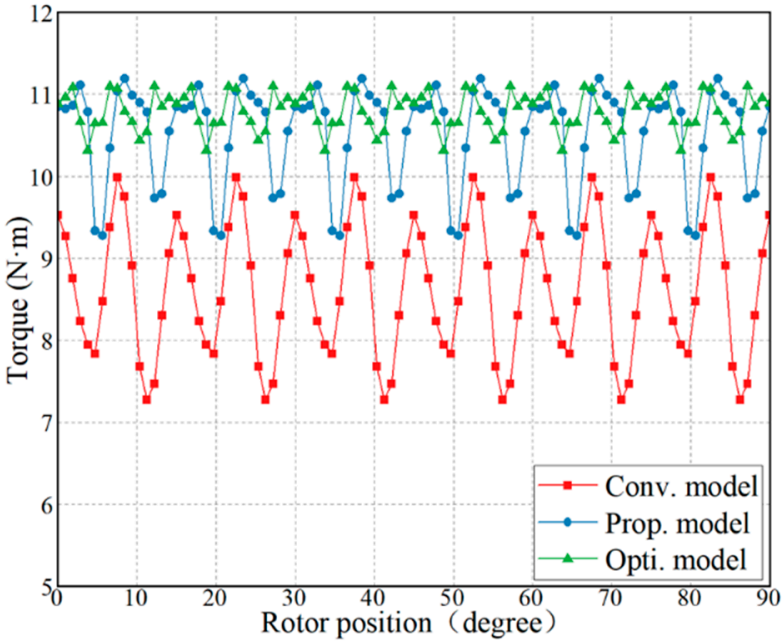

Figure 14. Comparison of the torque of the three models.

Table 5. Output torque errors between finite element simulation results and experimental results.

Reference	12	14	30	31
Error	2.71%	0.52%	4%	4.5%

4. Constant Power Speed Range Performance and Anti-Demagnetization Performance

The constant power speed range performance and the anti-demagnetization performance of the three models are compared and analyzed.

4.1. Constant Power Speed Range Performance Comparison

For PMA-SynRMs, wide constant power speed range performance (CPSR) is as important as high torque, high power density, and high efficiency. Comparison of torque–speed and power–speed curves for the three models is shown in Figure 15, and comparison of speed–efficiency plots is shown in Figure 16. In the calculation, the peak current is set to 7.07A. All three models use maximum torque per ampere (MTPA) control and flux-weakening (FW) control. As shown in Figure 15a, the proposed and optimized models exhibit higher torque in the constant torque region compared to the conventional model. From Figure 15b, it can be seen that the power of the conventional model starts decreasing after 2000 rpm, while the power of the proposed and optimized models starts decreasing after 3500 rpm. This demonstrates that the proposed and optimized models have higher power density compared to the conventional model. From Figure 16, it can be seen that the efficiency of the proposed and optimized models is slightly higher than that of the conventional model in the low speed range and slightly lower than that of the conventional model in the high speed range. In conclusion, the proposed and optimized models have better CPSR performance compared to the conventional model.

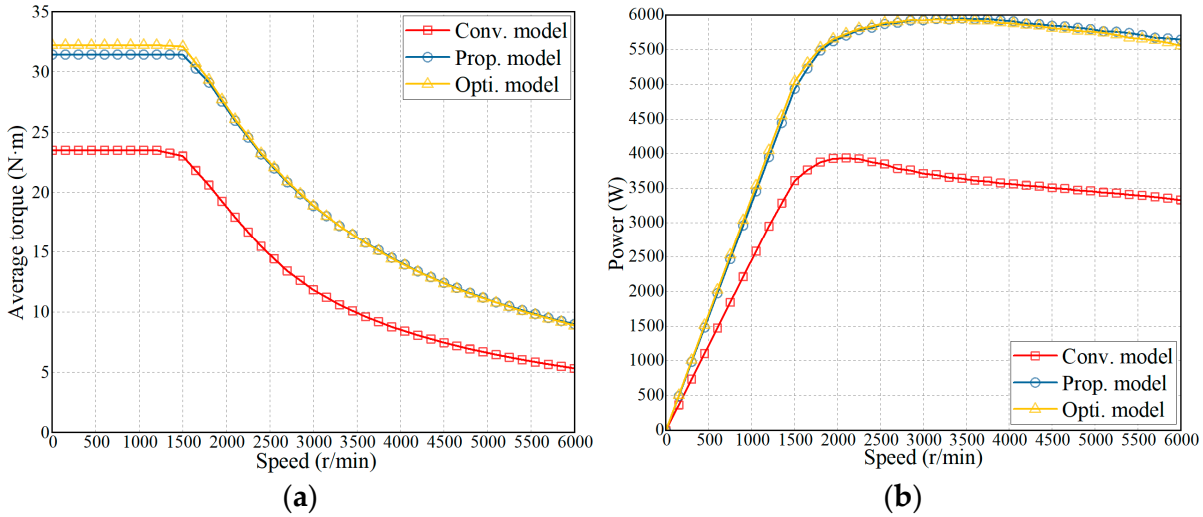

Figure 15. Comparison of the torque–speed and power–speed curves for the three models. (**a**) Torque–speed. (**b**) Power–speed.

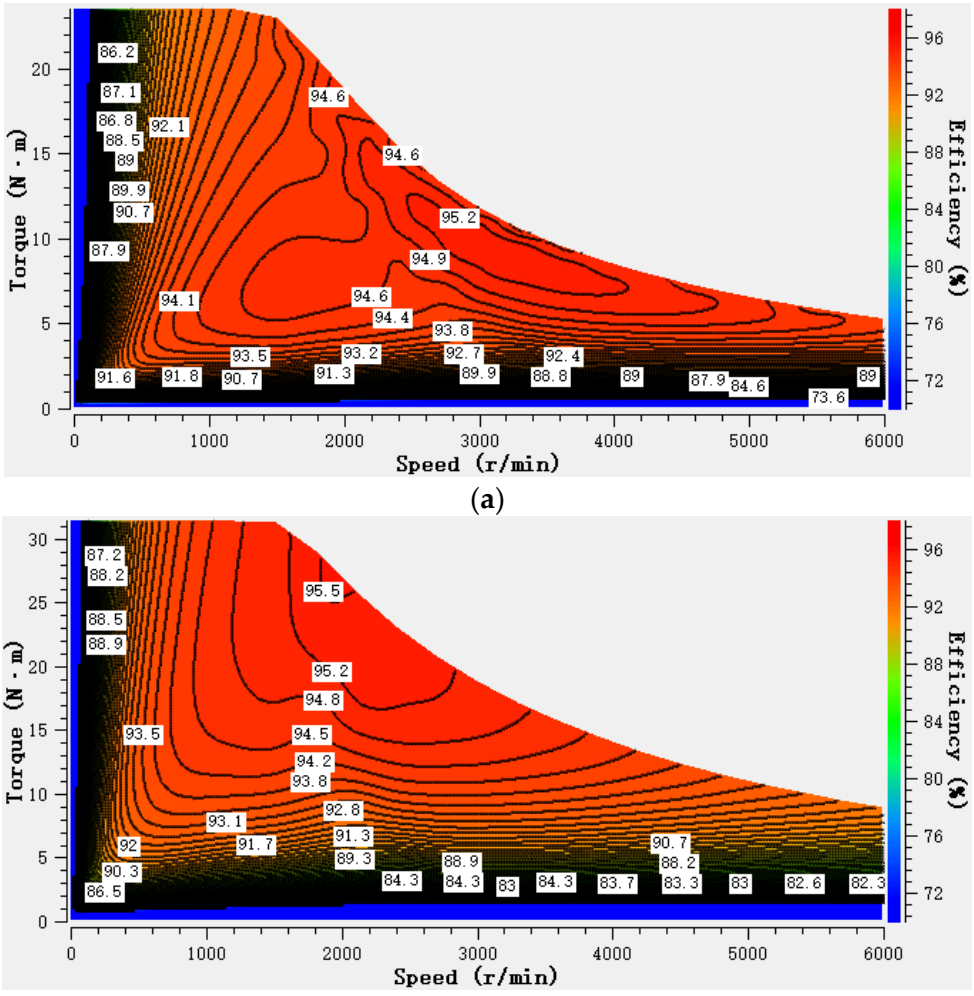

Figure 16. *Cont.*

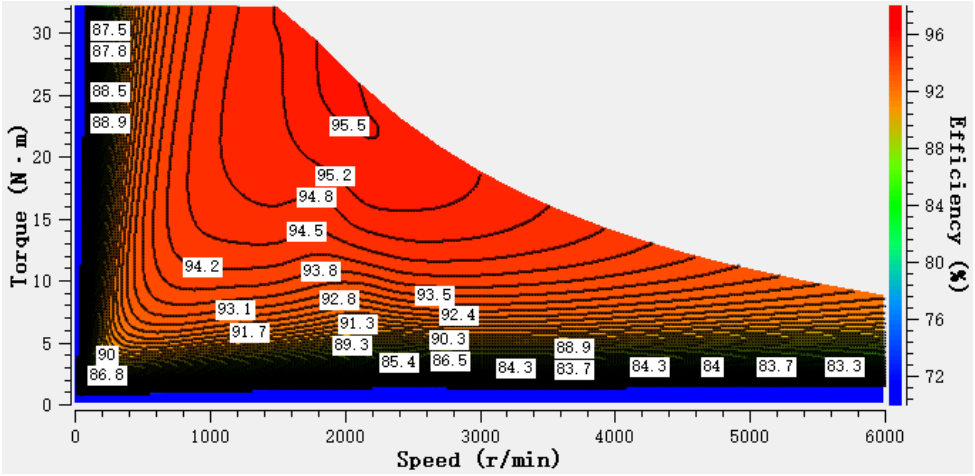

(**c**)

Figure 16. Speed–efficiency comparison of the three models. (**a**) Conventional model. (**b**) Proposed model. (**c**) Optimized model.

4.2. Comparison of Anti-Demagnetization Performance

Permanent magnets with smaller size are usually more prone to demagnetization. Since the proposed and optimized models in this paper use multilayer and smaller-sized permanent magnets, it is necessary to analyze the anti-demagnetization performance of the three models. The demagnetization of permanent magnets is analyzed by examining the changes in remanence of permanent magnets before and after applying high input currents. The definition formula for demagnetization rate [32] is shown in Equation (12).

$$\delta = \left(1 - \frac{B_r'}{B_r}\right) \times 100\% \tag{12}$$

where B_r' is the remanence of the permanent magnet after a high input current, and B_r is the remanence of permanent magnets in the initial state.

When the control temperature is 170 °C and 200 °C, the maximum controlled input current is nine times the rated current. The maximum demagnetization rates of the permanent magnets for the three models under different input current conditions are shown in Figure 17. Figure 17a compares the maximum demagnetization rate of the three models with different input currents at 170 °C. The maximum demagnetization rate of all three models is less than 1%, indicating minimal demagnetization. It is shown that the three models have good anti-demagnetization performance under extreme operating conditions. Figure 17b shows the comparison of the maximum demagnetization rate of the three models with different input currents at 200 °C. At four times the rated current, the permanent magnets of the proposed and optimized models start to demagnetize. Compared to the proposed model and the optimized model, the permanent magnet of the conventional model has a larger size and a stronger anti-demagnetization performance. In Table 6, it can be seen that the maximum demagnetization rate of the optimized model is reduced by 13.84% compared to the proposed model at a temperature of 200 °C and nine times the rated current operating condition. This indicates that the anti-demagnetization performance of the optimized model is improved compared to the proposed model. Figure 18 shows the demagnetization rate distributions of the three models at a temperature of 200 °C and an input current of nine times the rated current.

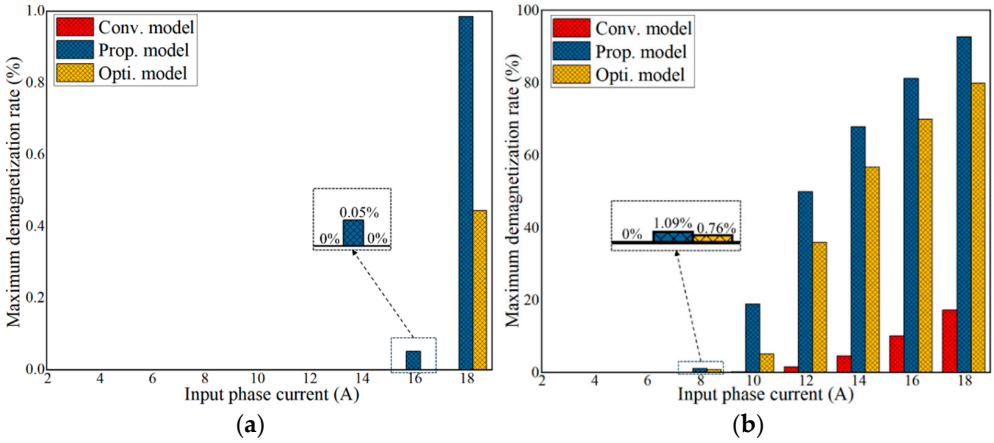

Figure 17. Maximum demagnetization rates for the three models with different input currents. (**a**) For input of 170 °C. (**b**) For input of 200 °C.

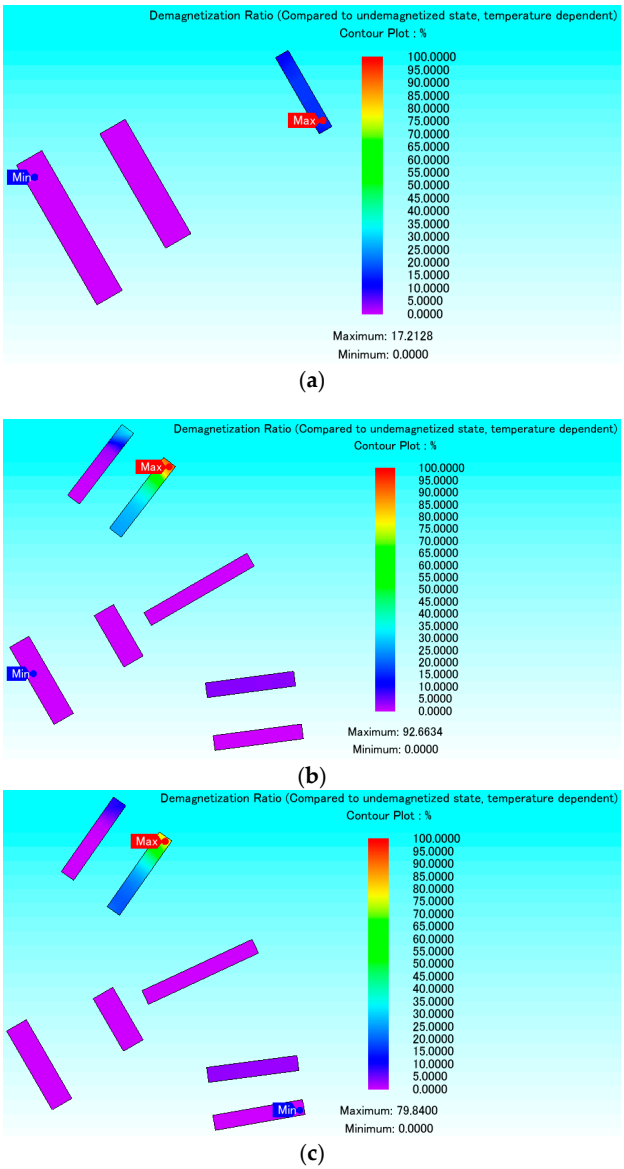

Figure 18. Demagnetization rate distribution plots for the three models at 200 °C and nine times the input current. (**a**) Conventional model. (**b**) Proposed model. (**c**) Optimized model.

Table 6. Maximum demagnetization rate of three models of permanent magnets under operating conditions at different temperatures and nine times the rated current.

Temperature	Unit	Conv. Model	Prop. Model	Opti. Model
170 °C	%	0	0.98	0.44
200 °C	%	17.21	92.66	79.84

5. Conclusions

In this paper, a conventional PMA-SynRM is used as a reference for study. An asymmetric-rotor PMA-SynRM combined with a Halbach array is proposed using the same amount of permanent magnets. The torque characteristics of both models are theoretically analyzed by establishing a simplified analytical model of the conventional model and the proposed model, neglecting core saturation and cross-coupling. No-load simulation analysis reveals that the permanent magnet flux linkage of the proposed model is shifted, resulting in significantly increased air-gap magnetization compared to the conventional model. Load simulation analysis indicates that the proposed model achieves higher utilization of permanent magnet torque and reluctance torque utilization, leading to a notable improvement in average torque. Furthermore, through optimal design, sensitivity analysis, and multi-objective optimization, the average torque of the optimized model is increased and the torque ripple is reduced compared to the conventional model. Finally, the CPSR performance and anti-demagnetization performance of the three models are analyzed. CPSR comparison results demonstrate that both the proposed and optimized models exhibit superior performance. In the analysis of the anti-demagnetization performance, it is found that at a set temperature of 170 °C and under nine times the maximum rated current, all three models show minimal demagnetization, indicating robust anti-demagnetization capabilities. However, at 200 °C and under the same current conditions, the proposed model shows the most severe demagnetization rate of the permanent magnets, while the conventional model shows the lowest demagnetization rate of the permanent magnets. This highlights that the conventional model outperforms the other in terms of anti-demagnetization performance, whereas the proposed model demonstrates poorer anti-demagnetization performance. Compared with the conventional model, the permanent magnet of the proposed model is more prone to demagnetization at high temperatures. Therefore, in the subsequent research, the temperature rise design should be given focus to prevent the demagnetization of the permanent magnet at excessive temperature.

Author Contributions: Conceptualization, F.X.; methodology, F.X.; software, J.Z.; validation, J.Z.; formal analysis, J.Z.; investigation, F.X.; resources, C.Q.; data curation, J.Z. and M.Z; writing—original draft preparation, J.Z.; writing—review and editing, F.X.; visualization, J.Z.; supervision, C.Q.; project administration, F.X.; funding acquisition, M.Z. and C.Q. All authors have read and agreed to the published version of the manuscript.

Funding: This research was in part supported by the Stable Funding Support for Universities in Shenzhen (GXWD20220817140906007) and the Start-up Funding for Newly Introduced Talents in Shenzhen (CA11409031).

Institutional Review Board Statement: Not applicable.

Informed Consent Statement: Not applicable.

Data Availability Statement: The original contributions presented in the study are included in the article, further inquiries can be directed to the corresponding author.

Conflicts of Interest: The authors declare no conflicts of interest.

References

1. Shen, J.X.; Lin, Y.Q.; Sun, Y.; Qin, X.F.; Wan, W.J.; Cai, S. Permanent Magnet Synchronous Reluctance Machines with Axially Combined Rotor Structure. *IEEE Trans. Magn.* **2022**, *58*, 8103310. [CrossRef]
2. Zhao, W.; Xing, F.; Wang, X.; Lipo, T.A.; Kwon, B.I. Design and Analysis of a Novel PM-Assisted Synchronous Reluctance Machine with Axially Integrated Magnets by the Finite-Element Method. *IEEE Trans. Magn.* **2017**, *53*, 8104104. [CrossRef]
3. Mohammadi, A.; Mirimani, S.M. Design of a Novel PM-Assisted Synchronous Reluctance Motor Topology Using V-Shape Permanent Magnets for Improvement of Torque Characteristic. *IEEE Trans. Eng. Conv.* **2022**, *37*, 424–432. [CrossRef]
4. Bianchi, N.; Fornasiero, E.; Soong, W. Selection of PM Flux Linkage for Maximum Low-Speed Torque Rating in a PM-Assisted Synchronous Reluctance Machine. *IEEE Trans. Ind. Appl.* **2015**, *51*, 3600–3608. [CrossRef]
5. Barcaro, M.; Bianchi, N.; Magnussen, F. Permanent-Magnet Optimization in Permanent-Magnet-Assisted Synchronous Reluctance Motor for a Wide Constant-Power Speed Range. *IEEE Trans. Ind. Electron.* **2012**, *59*, 2495–2502. [CrossRef]
6. Bianchi, N.; Fornasiero, E.; Ferrari, M.; Castiello, M. Experimental Comparison of PM-Assisted Synchronous Reluctance Motors. *IEEE Trans. Ind. Appl.* **2016**, *52*, 163–171. [CrossRef]
7. Nobahari, A.; Vahedi, A.; Nasiri-Zarandi, R. A Modified Permanent Magnet-Assisted Synchronous Reluctance Motor Design for Torque Characteristics Improvement. *IEEE Trans. Eng. Conv.* **2022**, *37*, 989–998. [CrossRef]
8. Lu, Y.; Li, J.; Xu, H.W.; Yang, K.; Xiong, F.; Qu, R.H.; Sun, J.B. Comparative Study on Vibration Behaviors of Permanent Magnet Assisted Synchronous Reluctance Machines with Different Rotor Topologies. *IEEE Trans. Ind. Appl.* **2021**, *57*, 1420–1428. [CrossRef]
9. Lazari, P.; Wang, J.; Sen, B. 3-D Effects of Rotor Step-Skews in Permanent Magnet-Assisted Synchronous Reluctance Machines. *IEEE Trans. Magn.* **2015**, *51*, 8112704. [CrossRef]
10. Islam, M.Z.; Arafat, A.; Bonthu, S.S.R.; Choi, S. Design of a Robust Five-Phase Ferrite-Assisted Synchronous Reluctance Motor with Low Demagnetization and Mechanical Deformation. *IEEE Trans. Eng. Conv.* **2019**, *34*, 722–730. [CrossRef]
11. Obata, M.; Morimoto, S.; Sanada, M.; Inoue, Y. Performance of PMASynRM With Ferrite Magnets for EV/HEV Applications Considering Productivity. *IEEE Trans. Ind. Appl.* **2014**, *50*, 2427–2435. [CrossRef]
12. Payza, O.; Demir, Y.; Aydin, M. Investigation of Losses for a Concentrated Winding High-Speed Permanent Magnet-Assisted Synchronous Reluctance Motor for Washing Machine Application. *IEEE Trans. Magn.* **2018**, *54*, 8207606. [CrossRef]
13. Jamali-Fard, A.; Mirsalim, M. Design and Prototyping of a Novel Line-Start Permanent Magnet Assisted Synchronous Reluctance Motor for Fan Application. *IEEE Trans. Eng. Conv.* **2024**, *39*, 243–251. [CrossRef]
14. Degano, M.; Murataliyev, M.; Shuo, W.; Barater, D.; Buticchi, G.; Jara, W.; Bianchi, N.; Galea, M.; Gerada, C. Optimised Design of Permanent Magnet Assisted Synchronous Reluctance Machines for Household Appliances. *IEEE Trans. Eng. Conv.* **2021**, *36*, 3084–3095. [CrossRef]
15. Bianchi, N.; Bolognani, S.; Carraro, E.; Castiello, M.; Fornasiero, E. Electric Vehicle Traction Based on Synchronous Reluctance Motors. *IEEE Trans. Ind. Appl.* **2016**, *52*, 4762–4769. [CrossRef]
16. Gowtham, V.; Nikhitha, A.; Sashidhar, S. Current Advance Angle-Based Rare-Earth-Free Hybrid PMa-SyRM Drive Using Hall-Sensors for an Air-Conditioner Compressor. *IEEE Access* **2023**, *11*, 115924–115933. [CrossRef]
17. Abhijith, V.; Hossain, M.J.; Lei, G.; Sreelekha, P.A.; Kadam, S.B. High Torque Capability Non-Permanent Magnet Hybrid Excited Switched Reluctance Motor for Electric Vehicle Application. In Proceedings of the 2023 IEEE Energy Conversion Congress and Exposition (ECCE), Nashville, TN, USA, 29 October–2 November 2023; pp. 3851–3858.
18. Niazi, P.; Toliyat, H.A.; Cheong, D.H.; Kim, J.C. A Low-Cost and Efficient Permanent-Magnet-Assisted Synchronous Reluctance Motor Drive. *IEEE Trans. Ind. Appl.* **2007**, *43*, 542–550. [CrossRef]
19. Zhao, W.; Xing, F.; Wang, X.; Lipo, T.A.; Kwon, B.I. Optimal Design of a Novel V-Type Interior Permanent Magnet Motor with Assisted Barriers for the Improvement of Torque Characteristics. *IEEE Trans. Magn.* **2014**, *50*, 8104504. [CrossRef]
20. Maroufian, S.S.; Pillay, P. Design and Analysis of a Novel PM-Assisted Synchronous Reluctance Machine Topology with AlNiCo Magnets. *IEEE Trans. Ind. Appl.* **2019**, *55*, 4733–4742. [CrossRef]
21. Kondo, K.; Kusase, S.; Maekawa, T.; Hanada, K. A New PM-Assisted Synchronous Reluctance Motor with Three-Dimensional Trench Air Gap. *IEEE Trans. Ind. Appl.* **2014**, *50*, 2485–2492. [CrossRef]
22. Bianchi, N.; Bolognani, S.; Bon, D.; Dai PrÉ, M. Torque Harmonic Compensation in a Synchronous Reluctance Motor. *IEEE Trans. Eng. Conv.* **2008**, *23*, 466–473. [CrossRef]
23. Ngo, D.K.; Hsieh, M.F.; Huynh, T.A. Torque Enhancement for a Novel Flux Intensifying PMa-SynRM Using Surface-Inset Permanent Magnet. *IEEE Trans. Magn.* **2019**, *55*, 8106108. [CrossRef]
24. Amin, M.; Aziz, G.A.A. Hybrid Adopted Materials in Permanent Magnet-Assisted Synchronous Reluctance Motor with Rotating Losses Computation. *IEEE Trans. Magn.* **2019**, *55*, 8103305. [CrossRef]
25. Liu, H.C.; Kim, I.G.; Oh, Y.J.; Lee, J.; Go, S.C. Design of Permanent Magnet-Assisted Synchronous Reluctance Motor for Maximized Back-EMF and Torque Ripple Reduction. *IEEE Trans. Magn.* **2017**, *53*, 8202604. [CrossRef]
26. Diao, C.; Zhao, W.; Liu, Y.; Wang, X. Permanent Magnet Assisted Synchronous Reluctance Motor with Asymmetric Rotor for High Torque Performance. *CES Trans. Electron. Mach. Syst.* **2023**, *7*, 179–186. [CrossRef]
27. Xie, Y.; Shao, J.; He, S.; Ye, B.; Yang, F.; Wang, L. Novel PM-Assisted Synchronous Reluctance Machines Using Asymmetrical Rotor Configuration. *IEEE Access* **2022**, *10*, 79564–79573. [CrossRef]

28. Li, G. A Pearson Based Feature Compressing Model for SNARE Protein Classification. *IEEE Access* **2020**, *8*, 136560–136569. [CrossRef]
29. Llopis-Albert, C.; Rubio, F.; Zeng, S. Multiobjective Optimization Framework for Designing A Vehicle Suspension System. A Comparison of Optimization Algorithms. *Adv. Eng. Softw.* **2023**, *176*, 103375. [CrossRef]
30. Nasiri-Zarandi, R.; Karami-Shahnani, A.; Toulabi, M.S.; Tessarolo, A. Design and Experimental Performance Assessment of an Outer Rotor PM-Assisted SynRM for the Electric Bike Propulsion. *IEEE Trans. Ind. Electron.* **2023**, *9*, 727–736. [CrossRef]
31. Hua, Y.; Zhu, H.; Gao, M.; Ji, Z. Multiobjective Optimization Design of Permanent Magnet Assisted Bearingless Synchronous Reluctance Motor Using NSGA-II. *IEEE Trans. Ind. Electron.* **2021**, *68*, 10477–10487. [CrossRef]
32. Wang, K.; Li, J.; Zhu, S.S.; Liu, C. Novel Hybrid-Pole Rotors for Consequent-Pole PM Machines Without Unipolar Leakage Flux. *IEEE Trans. Ind. Electron.* **2019**, *66*, 6811–6823. [CrossRef]